

Supplementary document to

Rotary 4D Printing of Modular Elements on Sustainable 4D Mandrel

Hesam Soleimanzadeh¹, Mahdi Bodaghi², Marzieh Jamalabadi³, Bernard Rolfe¹, Ali Zolfagharian¹

¹School of Engineering, Deakin University, Geelong, Victoria 3216 Australia

²Department of Engineering, School of Science and Technology, Nottingham Trent University, Nottingham NG11 8NS, UK

³Institute for Intelligent Systems Research and Innovation (IISRI), Deakin University, Geelong, Victoria 3216 Australia

Supplementary Note 1: Parametric re-entrant NURBS auxetic metamaterial design

To design the bio-inspired re-entrant NURBS auxetic metamaterial, we employed seven control points $P_{i=0,1,2,\dots,7}$ (Figure 1) to define a clamped cubic NURBS curve, denoted as $C(u)$, for both ends. The NURBS curve is constructed with 11 knot points, as specified below, to control the shape and flexibility of the structure. Furthermore, to ensure an optimal smooth curve throughout the design, all weight points are uniformly set to 1, enabling consistent control over the curve's geometry while maintaining the integrity of the auxetic pattern. This method ensures precise manipulation of the auxetic metamaterial's shape and mechanical properties.

$$C(u) = \frac{\sum_{i=1}^7 N_{i,3}(u) \cdot P_i}{\sum_{i=1}^7 N_{i,3}(u)} \text{ where } N_{i,0}(u) = \begin{cases} 1 & \text{if } u_i \leq u \leq u_{i+1} \\ 0 & \text{Otherwise} \end{cases},$$
$$N_{i,1}(u) = \frac{u - u_i}{u_{i+1} - u_i} N_{i,0}(u) + \frac{u_{i+2} - u}{u_{i+2} - u_{i+1}} N_{i+1,0}(u),$$
$$N_{i,2}(u) = \frac{u - u_i}{u_{i+2} - u_i} N_{i,1}(u) + \frac{u_{i+3} - u}{u_{i+3} - u_{i+1}} N_{i+1,1}(u), \quad (S1)$$
$$N_{i,3}(u) = \frac{u - u_i}{u_{i+3} - u_i} N_{i,2}(u) + \frac{u_{i+4} - u}{u_{i+4} - u_{i+1}} N_{i+1,2}(u),$$
$$\text{Knot Vector: } [0,0,0,0,1,2,3,4,4,4,4]$$

where for each control point, the following condition applies:

$$P_1 \begin{cases} p_1^x = O^x + \frac{\bar{V}_1 L_x^n}{2} + P_t \\ p_1^y = O^y + L_y - \frac{P_t}{2} \end{cases}; P_2 \begin{cases} p_2^x = p_1^x \\ p_2^y = O^y + L_y \left(1 - \frac{\bar{V}_2}{4}\right) \end{cases}; P_3 \begin{cases} p_3^x = O^x + \frac{L_x^n}{2} (1 - \bar{V}_1) + p_t \\ p_3^y = O^y + \frac{L_y}{2} \left(1 + \frac{\bar{V}_2}{2}\right) \end{cases} \quad (S2)$$
$$P_4 \begin{cases} p_4^x = p_3^x \\ p_4^y = O^y + \frac{L_y}{2} \end{cases}; P_5 \begin{cases} p_5^x = p_3^x \\ p_5^y = O^y + \frac{L_y}{2} \left(1 - \frac{\bar{V}_2}{2}\right) \end{cases}; P_6 \begin{cases} p_6^x = p_1^x \\ p_6^y = O^y + \frac{\bar{V}_2 L_y}{4} + \frac{P_t}{2} \end{cases}; P_7 \begin{cases} p_7^x = p_1^x \\ p_7^y = O^y + \frac{P_t}{2} \end{cases}$$

where $O(0,0,0)$ represents the origin coordinates of the flattened auxetic cell pattern.

Supplementary Note 2: Auxetic Metamaterials Relative Density

Since the mechanical properties of a structure are inherently linked to its relative density, it is essential to derive the expressions for relative density as a function of the arc length, which can be determined through the calculation outlined in **Equation 6**. This relationship will provide a more accurate characterization of the metamaterial's mechanical behavior based on its geometrical configuration.

$$A_a^n = -6P_t^2 + \left[6C_L + \frac{4\pi(D_p + 2P_h n)(1 - \bar{V}_1)}{N_x} \right] P_t \quad (S3)$$

$$V_a^n = \left[\frac{4\pi D_p P_t (1 - \bar{V}_1)}{N_x} + 6P_t C_L - 6P_t^2 \right] P_h n + \left[\frac{4\pi P_t (1 - \bar{V}_1)}{N_x} \right] P_h^2 n^2 \quad (S4)$$

$$V_{cell}^n = \left[\frac{\pi D_p L_y}{N_x} \right] P_h n + \left[\frac{\pi L_y}{N_x} \right] P_h^2 n^2 \quad (S5)$$

$$\bar{\rho}^n = \frac{V_a^n}{V_{cell}^n} \quad (S6)$$

where A_a^n , V_a^n , and $\bar{\rho}^n$ are the area, volume, and relative density of each auxetic pattern inside each cell of n^{th} layer, respectively.

Supplementary Note 3: Tubular G-code Algorithm

The algorithm consists of six key components, illustrated in **Supplementary Figure 1**: Inputs, Cylindrical Printing Bed, Pattern and Printing Path, NURBS Representation, Numerical Simulation, and G-code Generation, each outlined concisely below:

Inputs: This section contains a cluster named "*Parameters*" encompassing all essential printing details.

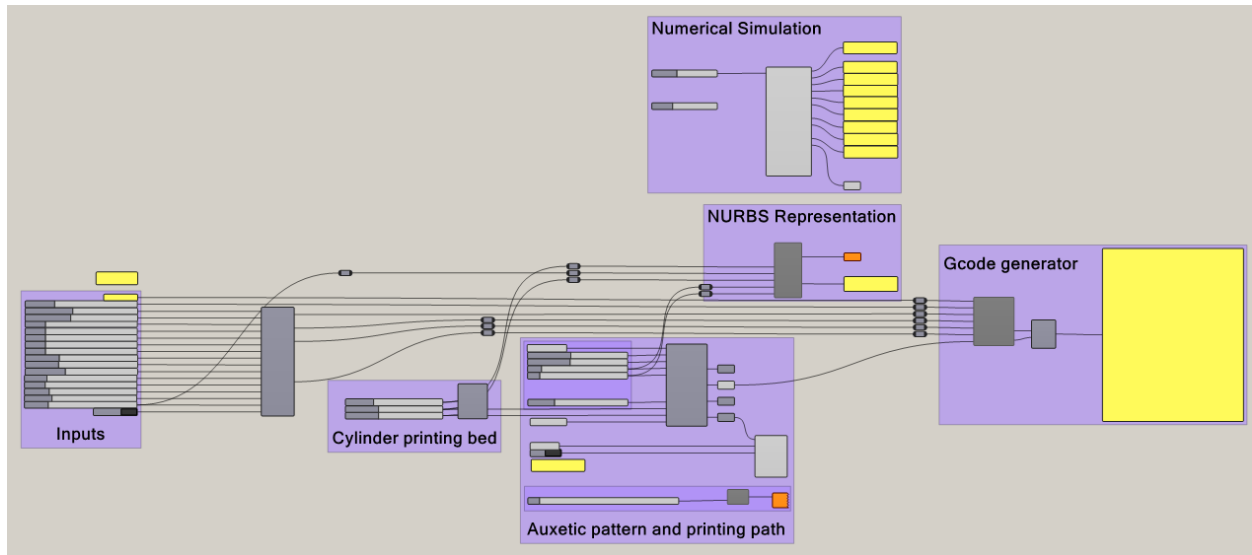
Cylindrical Printing Bed: This module enables users to configure a flattened printing platform, defining layer boundaries as design constraints. It includes a "*Flattened Pattern*" cluster, which accepts inputs like N_x , N_y , L_y origin, and platform radius to output boundary lines.

Pattern and Printing Path: Here, a flattened-cell design is established, specifically for a Re-entrant Auxetic pattern. This component comprises two clusters: "*Re-entrant Auxetic*" and "*Bake 3D*." The Re-entrant Auxetic cluster receives parameters \bar{V}_1 and \bar{V}_2 along with precision and representation options, generating auxetic cells and transferring NURBS curves to path data for G-code preparation. The Bake 3D cluster utilizes the Auxetic cell and additional geometric dimensions to create a 3D cylindrical auxetic structure, ready for further analysis, such as FEA.

NURBS Representation: This section features an "*Auxetic NURBS*" cluster, which takes geometric dimensions as input to produce NURBS representations, serving as comparative values for numerical simulations.

Numerical Simulation: All numerical formulations needed to reduce the computational load of NURBS calculations are contained here, including the "*NURBS Approximation*" cluster.

G-code Generation: This module, featuring a "*G-code Generator*" cluster, accepts paths, printing parameters, and geometric dimensions to generate the G-code for the current layer, outputting the G-code and final extrusion value for that layer.



Supplementary Figure 1 *Tubular G-code generator grasshopper algorithm workflow.*

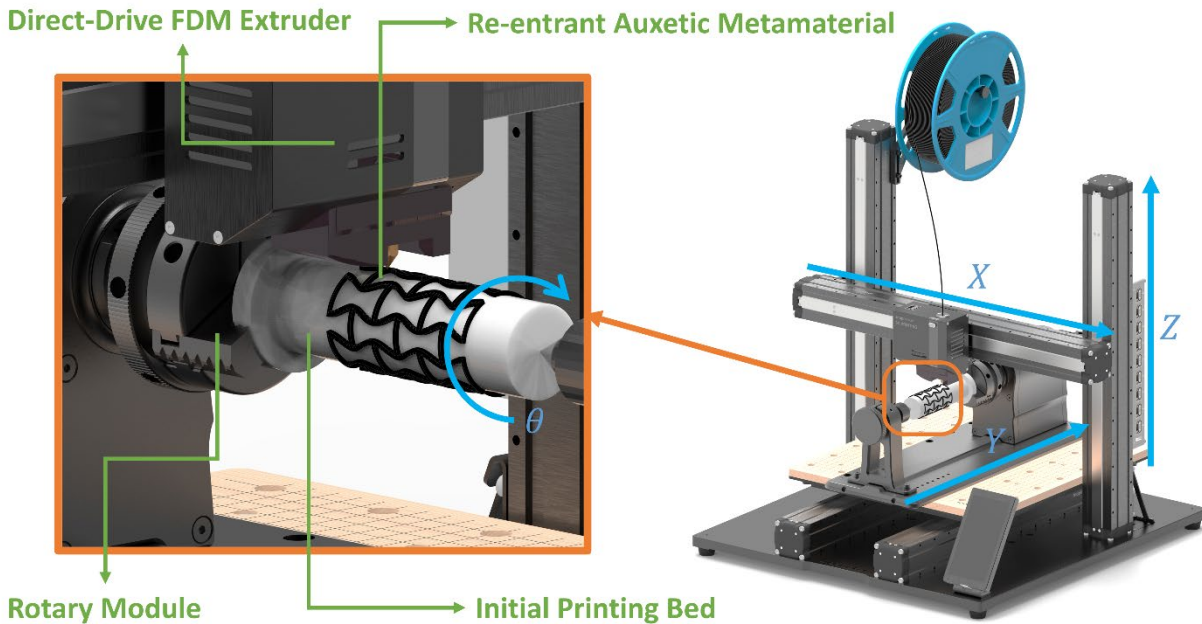
Supplementary Note 4: Fabrication Process

A commercially available FDM 3D printer (Snapmaker 2.0 A350 3-in-1), as shown in **Supplementary Figure 2**, was utilized for the fabrication of all test specimens. No hardware modifications were made to the printer; instead, the rotary module, originally designed for CNC and laser cutting applications, was employed to facilitate controlled angular movements. This approach ensures that the methodology is easily replicable, enabling hobbyists and researchers alike to employ the same setup for fabricating cylindrical re-entrant auxetic honeycomb structures.

The rotary module, featuring strain wave gearing with a 100:1 speed reduction ratio, enables high-precision rotation with a minimum angular resolution of 0.1° . For the initial 3D printing stage, a cylindrical platform composed of acrylonitrile butadiene styrene (ABS) was printed with integrated gauge features to aid in centering the platform on the rotary chuck. To further enhance the adhesion between the specimens and the rotating shaft, adhesive tapes were applied to the cylindrical platform's surface, ensuring stability during the fabrication process. The non-planar fabrication process of auxetic honeycomb re-entrant can be seen from **Supplementary Video 1**

and 2. This setup ensures consistent, repeatable results, critical for experiments involving multi-stiffness auxetic designs. To ensure proper adhesion and accurate printing on the platform, it is essential to level the printing head with the platform. This can be achieved by manually positioning the printing head at the center of the platform and using the G92 command to set the origin of the local coordinate system. This process ensures precise calibration and alignment, which is critical for successful printing.

All specimens were fabricated using PLA filament supplied by Snapmaker, with a diameter of 1.75 mm and a density of 1.24 g/cm³. The filament is commercially sustainable, as it is derived and purified from corn grain, making it biodegradable and environmentally friendly. This choice of filament ensures a completely sustainable fabrication process without utilizing support materials. A small pattern auxetic 3D printed metamaterial with abovementioned algorithm can be seen from **Supplementary Video 3**.

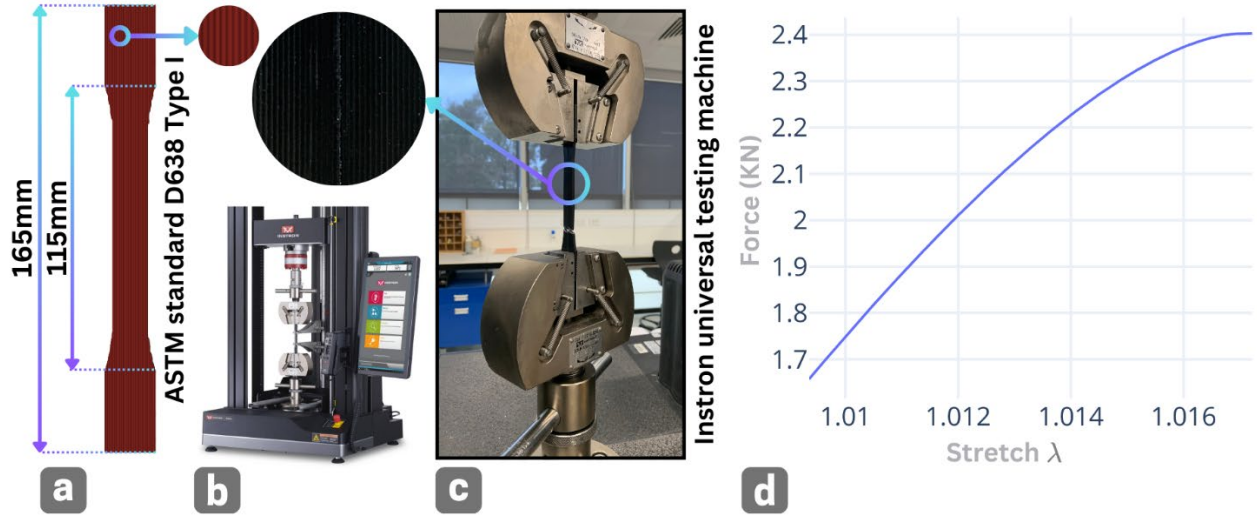


Supplementary Figure 2 Configuration and integration of a commercial FDM 3D printer with a rotary module for enhanced fabrication flexibility.

Supplementary Note 5: Material Characterization

To characterize the instantaneous and time-dependent behavior of PLA, a series of specimens were fabricated with a 0-degree orientation and 100% infill, using printing parameters consistent with those applied in our experimental setup. Since the tubular printing in this study is continuous and utilizes a 100% infill, all specimens were 3D printed with the PLA polymer orientation aligned to match the re-entrant auxetic shape, as depicted in **Supplementary Figure 3a**. The specimens were designed according to ASTM standard D-638 Type I, ensuring consistency in mechanical testing. Prior to conducting the mechanical tests, all specimens were stored in a dehydrator at

40 °C with continuous air circulation to minimize moisture absorption, ensuring uniform material properties during testing. The tensile tests were conducted using a universal Instron tensile testing machine, as shown in **Supplementary Figure 3b**, under ambient conditions, with a controlled strain rate of 2 mm/min. At this strain rate, both loading and unloading cycles were performed to verify the material's elastic behavior. The consistency of force-displacement curves across repeated trials confirmed that the material exhibited purely elastic properties. Additionally, the strain rate was sufficiently low to minimize any viscoelastic or inertial effects, ensuring accurate characterization of the material's mechanical response.



Supplementary Figure 3. Tensile test configuration and setup: (a) Dimensions of the ASTM D638 standard tensile specimen. (b) Universal testing machine (Instron) used for tensile testing. (c) Test configuration for determining the yield strength of PLA specimens. (d) Average force-displacement curve obtained from tensile tests of PLA specimens.

Ten specimens were printed based on the dimensions and printing parameters provided in **Supplementary Table 1**. The average force-displacement curve was then calculated using data obtained from the tensile test experiments, as shown in **Supplementary Figure 3d**. Now, we will derive the equations needed for fitting the hyperelastic and hyperfoam constants to experimental test data. In addition, for the hyperelastic models' full incompressibility is assumed in fitting the hyperelastic constants to the test data. The Yeoh model's expression for the strain energy function can be expressed as:

$$W = \sum_{i=1}^N C_{i0} (\bar{I}_1 - 3)^i + \sum_{i=1}^N \frac{1}{D_i} (J - 1)^{2i} \quad (s7)$$

where for the Yeoh model $N=3$, and $J = \bar{I}_3$ represents the modified third invariant of the Cauchy-Green deformation tensor, and assuming that PLA is incompressible, $J = 1$. This assumption simplifies the model by disregarding volumetric changes during deformation, which is valid for

incompressible materials like PLA when analyzing the stress-strain behavior in the calculation of curve lengths presented in **Equation (6)**.

Supplementary Table 1 Process and geometry parameters used in designing and slicer setting for 3D printing of specimens.

Process Parameters	Value	Geometry Parameters	Value
Layer Height	0.2 mm	Overall Length	165 mm
Layer Thickness	0.2 mm	Length of Narrow Section	57 mm
Printing Temperature	210 °C	Distance Between Grips	115 mm
Bed Temperature	60 °C	Gage Length	50 mm
Feed Rate	50 mm/s	Overall Width	19 mm
		Width of Narrow Section	13 mm
		Radius of Fillet	76 mm
		Thickness	3.2 mm

In the case of a uniaxial tensile test, it can be shown that,

$$\lambda_1 = \lambda_u \text{ and } \lambda_2 = \lambda_3 = \lambda_u^{-\frac{1}{2}} \quad (\text{s8})$$

where λ_u are values obtained from the graph in **Supplementary Figure 3d** during the deformation. Then, invariant of the Cauchy-Green deformation tensor can be computed as:

$$\bar{I}_1 = \lambda_u^2 + \frac{2}{\lambda_u} \quad (\text{s9})$$

The First Piola-Kirchhoff stress tensor towards samples longitudinal direction, derived from the Yeoh strain energy function, can be expressed as follows:

$$P_u = \sum_{i=1}^3 C_{i0} 2i (\lambda_u - \lambda_u^{-2}) (\bar{I}_1 - 3)^{i-1} = \sum_{i=1}^3 C_{i0} X_i(\lambda_u) \quad (\text{s10})$$

Given experimental data, the material constants are determined through a least-squares-fit procedure, which aims to minimize the relative error in stress. For n nominal stress–nominal strain data pairs, the error measure E is defined as:

$$E = \sum_{i=1}^n \left(\frac{P_{exp,i} - P_{u,i}}{P_{exp,i}} \right)^2 \quad (\text{s11})$$

After substituting **Equation (s10)** into **Equation (s11)**, and performing the minimization of **Equation (s11)** with respect to the material coefficient C_{i0} , the following condition is obtained:

$$\sum_{k=1}^n \sum_{i=1}^3 \frac{X_i(\lambda_k) X_j(\lambda_k)}{(P_{exp,k})^2} C_{i0} = \sum_{k=1}^n \frac{X_j(\lambda_k)}{P_{exp,k}}, \quad j = 1, 2, 3 \quad (\text{s12})$$

After solving the aforementioned system of equations to determine the coefficients C_{i0} , the resulting coefficients are listed in **Supplementary Table 2**. These values represent the PLA constants that provide the best fit to the experimental data within the framework of the Yeoh strain energy model being used. The coefficients were obtained by minimizing the relative error between the experimental and model-predicted stresses, ensuring an optimal representation of the PLA behavior.

Supplementary Table 2 Material parameters of Yeoh hyperelastic model for PLA 100% infill ratio.

Parameters	Value
C_{10}	5.29e2 MPa
C_{20}	-5.33e5 MPa
C_{30}	6.32e8 MPa

To account for the viscoelastic behavior of PLA, a suitable mathematical model must be integrated with the Yeoh model to incorporate the material's time-dependent response. A key phenomenon observed during long-term loading is stress relaxation, where the material's stiffness, both deviatoric and volumetric, decreases while the strain remains constant. The Prony series is widely recognized as an effective mathematical formulation to describe this behavior, allowing for accurate modeling of the time-dependent reduction in stiffness during sustained deformation. Upon fitting storage modulus E' to a Prony series model, the long-term modulus E_0 , determined by DMA test, relaxation moduli e_n , and relaxation times τ_n were determined as:

Supplementary Table 3 The Prony series coefficients identified for PLA

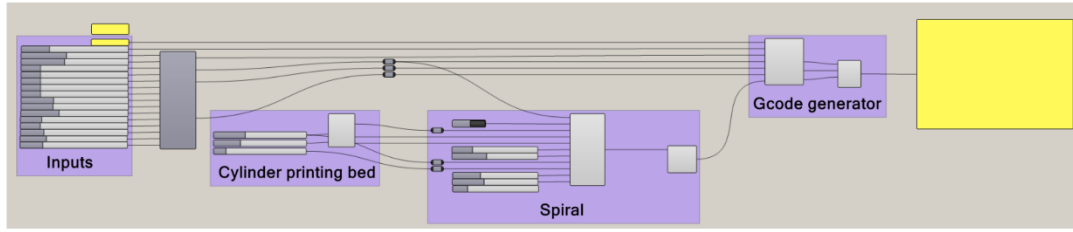
$\tau_n(s)$	$e_n(MPa)$	$\tau_n(s)$	$e_n(MPa)$	$\tau_n(s)$	$e_n(MPa)$
1e-11	0	1e-5	225.60	1e+1	51.82
1e-10	20.12	1e-4	292.64	1e+2	29.98
1e-9	50.31	1e-3	474.56	1e+3	14.40
1e-8	81.37	1e-2	449.43	1e+4	0.00
1e-7	97.02	1e-1	237.98	1e+5	0.72
1e-6	173.70	1e0	114.16		

The mechanical properties used as inputs for capturing the PLA's time-dependent response for the finite element analysis are detailed in **Supplementary Table 3**.

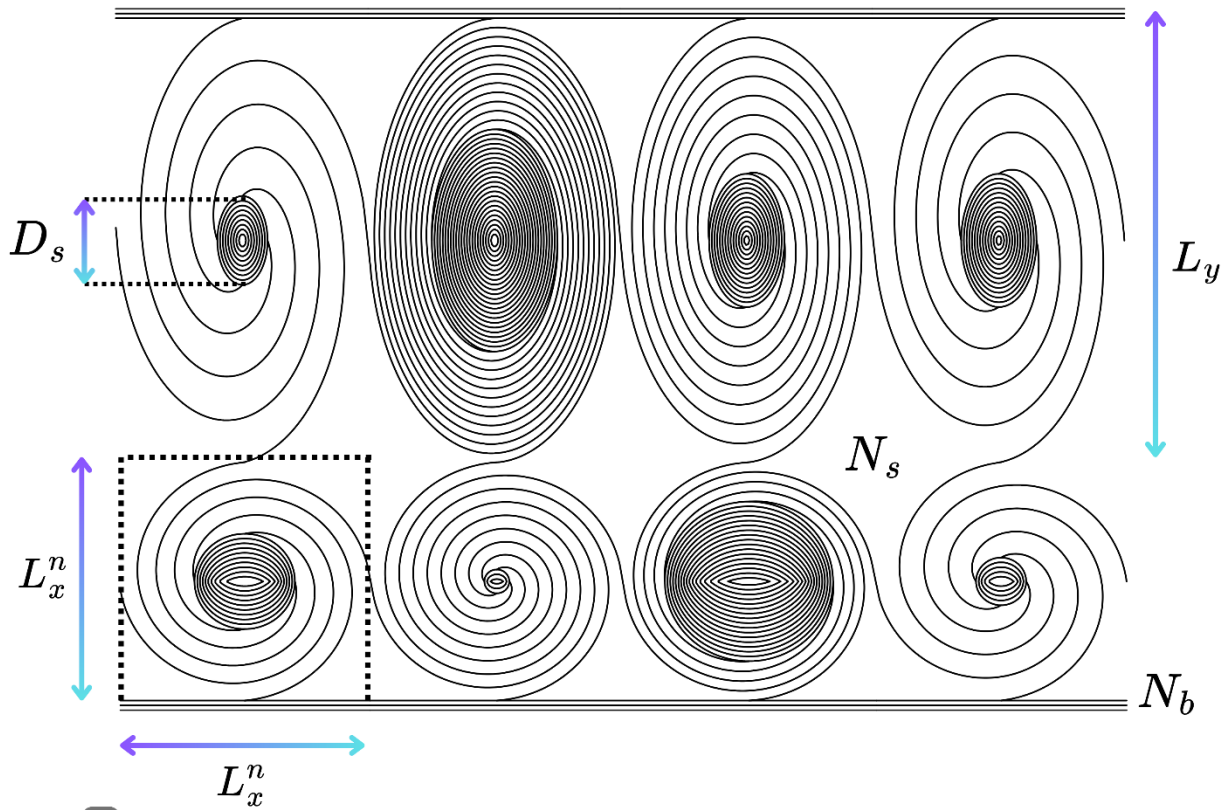
Supplementary Note 6: Poisson's Ratio

Given that we have one input variable and two dependent variables, and based on the assumption of incompressibility in hyperelastic materials, we can utilize the arc length of the curves, as described in **Equation 6**, as a constant throughout the deformation process. However, since there are two dependent variables, an additional condition is required to fully define the system. To address this, we are also aware of that the ligament length—the bar linking the auxetic shapes—remains constant during deformation. This assumption provides the necessary

constraints for maintaining consistency in the geometric relationships between the auxetic elements. Therefore, using predefined constraints, the Poisson's ratio for tunable re-entrant auxetic cells can be written as:



a



b

Supplementary Figure 4 (a) spiral G-code generator grasshopper algorithm workflow. (b) 2D gradient of spiral cell mapping using independent variables L_x^n , L_y , N_s , N_b , and D_s .

$$v = -\frac{\varepsilon_r}{\varepsilon_y} = -\frac{L_y(D'_L - D_L)}{D(L'_y - L_y)} \quad (s13)$$

where D'_L and L'_y are diameter and pattern height of deformed shape. Followingly, L'_y can be computed as:

$$L'_y = \frac{-A_2 - (A_2^2 - 4A_1A_3)^{1/2}}{2A_1} + P_t \quad (s14)$$

where:

$$A_1 = \frac{a_1^2}{(1 - a_1)^2} - 1; A_2 = \frac{2a_1^2Y - 2C_La_1}{(1 - a_1)^2} - 1; \text{ and } A_3 = \frac{C_L^2 + a_1^2Y^2 - 2C_La_1Y}{(1 - a_1)^2} - Y^2 \quad (s15)$$

$$a_1 = \frac{\bar{V}_2}{4}; a_2 = \frac{\pi}{N_x}; \text{ and } Y = \frac{2\pi}{N_x}D_L(1 - \bar{V}_1) - \frac{\pi D'_L}{N_x} \quad (s16)$$

And finally, the deformed \bar{V}_1' can be calculated as:

$$\bar{V}_1' = 1 - \frac{D_L(1 - \bar{V}_1)}{D'_L} \quad (s17)$$

Supplementary Note 7: Universal Spiral Joint Design Algorithm

The algorithm comprises four main components, detailed in **Supplementary Figure 4a**: Inputs, Cylindrical Printing Bed, Spiral, and G-code Generation. Three of these components are further explained in **Supplementary Note 3**. In this approach, the spiral cluster replaces the previous three re-entrant auxetic metamaterial clusters. This cluster takes specific inputs, including geometry dimensions, printing parameters, cell dimensions L_x^n and L_y , number of spirals N_s , number of borders N_b , and the center circle diameter ratio D_s (**Supplementary Figure 4b**). The output is a gradient of spiral cells, each tailored to different geometries, which enhances stiffness, maneuverability, and functional features.

As illustrated in **Supplementary Figure 4b**, there are two approaches for designing spiral cells. The first approach involves creating square cells, where the algorithm determines the number of repetitions in the x-direction by dividing it by the length of each cylindrical layer. In the second approach, the height of each cell can be customized through an additional input, allowing for variable cell heights. This flexibility enables the geometry to adapt to diverse deformation characteristics and parameters, enhancing the versatility of the design.